



Tailoring the coordination environment of cobalt in a single-atom catalyst through phosphorus doping for enhanced activation of peroxymonosulfate and thus efficient degradation of sulfadiazine

Yubin Zou^{a,b}, Jiahui Hu^{b,c}, Bing Li^{b,c,*}, Lin Lin^{b,c}, Yin Li^{b,c}, Feifei Liu^{b,c}, Xiao-yan Li^{a,b,d,*}

^a Shenzhen Environmental Science and New Energy Laboratory, Tsinghua-Berkeley Shenzhen Institute, Tsinghua University, Shenzhen, China

^b Shenzhen Engineering Research Laboratory for Sludge and Food Waste Treatment and Resource Recovery, Tsinghua Shenzhen International Graduate School, Tsinghua University, Shenzhen, China

^c Guangdong Provincial Engineering Research Centre for Urban Water Recycling and Environmental Safety, Tsinghua Shenzhen International Graduate School, Tsinghua University, Shenzhen, China

^d Environmental Engineering Research Centre, Department of Civil Engineering, The University of Hong Kong, Pokfulam, Hong Kong, China

ARTICLE INFO

Keywords:

PMS activation

Single-atom catalysts

Coordination environment

Organic degradation

Cobalt catalysts

ABSTRACT

The catalytic activity of single-atom catalysts (SACs) can be enhanced by engineering the coordination environment of metal centres. Herein, zeolitic imidazolate framework (ZIF) was used as a precursor to introduce P atoms into a Co-based SAC. With the P doping, the resultant ZIF-CoN₃P-C could efficiently degrade 98.4% of sulfadiazine (10 mg L⁻¹) within 5 min by activating peroxymonosulfate (PMS) with an elevated degradation rate constant 2.5 times that of ZIF-CoN₄-C. Density functional theory (DFT) calculations indicate that the electron density and electron delocalisation were further concentrated around the Co centres by the P doping, which facilitated electron transfer from Co to PMS molecules and enhanced the generation of singlet oxygen (¹O₂). The ZIF-CoN₃P-C exhibited its universality and stability for the PMS-based oxidation process. Overall, these findings clarify the role of P atoms in tuning the electronic structure and reactivity of Co in ZIF-CoN₃P-C for enhanced PMS activation and organic degradation.

1. Introduction

In recent decades, antibiotics have been overused in clinical and agricultural settings [1]. Overall, pharmaceutical plants, livestock farms, hospitals and households represent the major sources of antibiotics released into the environment [2]. Owing to antibiotic-mediated selection pressure, the numbers of antibiotic resistance bacteria and antibiotic resistance genes in bacteria are increasing, leading to growing public health concerns [3,4]. Therefore, the treatment of wastewater discharge that contains antibiotics from various sources has attracted increasing attention. However, conventional wastewater treatment facilities cannot efficiently eliminate antibiotics from treated effluent [5]. Thus, advanced technologies must be developed to overcome the challenge of antibiotic removal from wastewater. Sulphonamides (SAs) are a group of broad-spectrum antibiotics agents that are generally resistant to the physiochemical and biological treatments in wastewater

treatment plants [6]. Among SAs, sulfadiazine (SDZ) has been widely used, and its presence has been frequently detected in significant levels in the influents and effluents of wastewater treatment plants [7]. Thus, it is necessary to establish effective treatment methods to eliminate SAs and other antibiotics from wastewater before discharge.

Common advanced oxidation processes (AOPs), such as ozonation, chlorination and ultraviolet treatment, have high energy demands or generate toxic chlorine-substituted by-products, and thus may not be the optimal solutions for the antibiotics problem in water and wastewater [8,9]. Fenton reaction is a type of AOP that is widely implemented, owing to its ease of practical use and effective pollutant removal [10]. However, the chemical cost of Fenton reaction for wastewater treatment is high, and its high rate of sludge production may lead to a secondary pollution problem [11]. The hydrogen peroxide used in Fenton reaction can be replaced with persulfate as an oxidant, which reacts via a similar activation process, to help address these issues of Fenton reaction [12].

* Corresponding authors at: Shenzhen Engineering Research Laboratory for Sludge and Food Waste Treatment and Resource Recovery, Tsinghua Shenzhen International Graduate School, Tsinghua University, Shenzhen, China.

E-mail addresses: bingli@sz.tsinghua.edu.cn (B. Li), xlia@hku.hk (X.-y. Li).

<https://doi.org/10.1016/j.apcatb.2022.121408>

Received 4 February 2022; Received in revised form 29 March 2022; Accepted 10 April 2022

Available online 13 April 2022

0926-3373/© 2022 Elsevier B.V. All rights reserved.

Such persulfate-based AOPs, based on peroxydisulfate (PDS) or peroxymonosulfate (PMS), are not strictly dependent on solution pH and can generate a higher yield of various reactive oxygen species (ROS) [13]. Thus, reduced amounts of catalysts and chemicals would be used for these Fenton-like AOPs. Intensive effort has been made to decrease the catalyst consumption and waste production and enhance the reusability of the catalysts in persulfate-based AOPs by realising heterogeneous persulfate activation via solid-phase catalysts, such as metallic minerals, carbonaceous materials and their composites [14,15]. For SDZ degradation, multivalent Mn and Fe species in the MnS/Fe-MOF hybrid catalyst could accelerate the PMS activation [16]. Sulphur(II) in sulphide-modified zero-valent iron/PMS system could enhance the conversion of Fe^{3+} to Fe^{2+} in both liquid and solid phase, and promote SDZ removal within 10 min [17].

Considerable research has been performed on single-atom catalysts (SACs) since their introduction [18]. SACs, which are consist of single metal atom sites on a support, are different from traditional metal- (M-) or metal-oxide-based catalysts. The MN_4 sites were designed for SACs to narrow the gap between heterogeneous and homogeneous catalysis [19]. When single metal atoms are individually anchored onto a substrate, high atomic efficiencies and high surface energies can be realised, leading to enhanced catalytic performance for aqueous pollutant abatement and removal at a low cost [20]. The regulated coordination environments of SACs facilitate their specific interactions with various reactant molecules, thereby leading to selective catalytic reactions [21]. Moreover, the structural homogeneity of SACs can help to clarify their fundamental structure-activity relationships at the micro-level [22]. In PMS activation, interactions between PMS and various single atom sites would generate multiple ROS. Zhang et al. developed an Fe single-atom catalyst on carbon nitrate (Fe_1/CN) with a high Fe loading of 11.2 wt% that could generate $^1\text{O}_2$ selectively [23]. Besides, high-valent metals (e.g., Fe(V)=O and high-valent FeCo=O) were observed as the dominant reactive species in the Fe-SACs/PMS system when phenanthroline or formamide was used as the precursor of the catalyst [24,25].

Metal-organic frameworks (MOFs) have been identified as an ideal platform for the synthesis of SACs, given their well-defined structures and tuneable pores [26,27]. In particular, MOFs can enable the precise design and fabrication of SACs for enhanced Fenton-like reactions, as MOF-derived carbon materials can retain the framework of MOFs but exhibit considerably greater stability and conductivity. Owing to their intrinsic metal–nitrogen bonds, zeolitic imidazolate frameworks (ZIFs) are considered ideal precursors of SACs [28], and zinc (Zn)-based ZIF-8 can be used to realise one-step SAC synthesis by a host-guest strategy [29]. Through pyrolysis at 907 °C or higher temperatures, various guest metals (e.g., Mn, iron (Fe), Co, copper (Cu), silver, or platinum) can be introduced to replace the evaporated Zn sites in the host carbon framework [30–32]. Recently, ZIF-8-derived Fe-SACs were synthesised with abundant atomically dispersed Fe-N_x sites for PMS activation and singlet oxygen ($^1\text{O}_2$) production [33]. By controlling the Zn/Co molar ratio during the synthesis process, CoN_{2+2} sites could be constructed in the SACs, which promoted the catalytic conversion of PMS to $^1\text{O}_2$ for AOP [34].

However, it remains unclear how the presence of heteroatoms in the carbon support affects the coordination environment of metal atoms in the SACs and the resulting activation of PMS. Besides, developing an understanding of how to effectively control the coordination environment of metal atoms in SACs will enable the design and synthesis of high-performance SACs. Thus, in the present research, we introduced phosphorus (P) into Co-based SACs through the host-guest technique to construct $\text{Co-N}_3\text{P}$ sites, thereby forming a novel catalyst: ZIF- $\text{CoN}_3\text{P-C}$. The PMS-activation efficacy and reactivity of the ZIF- $\text{CoN}_3\text{P-C}$ were examined in terms of its ability to catalyse the degradation of SDZ. The high efficacy of ZIF- $\text{CoN}_3\text{P-C}$ was compared with that of various structural analogues, such as ZIF-C, ZIF-P-C and ZIF- $\text{CoN}_4\text{-C}$. The predominant ROS in the ZIF-derived catalyst/PMS systems were determined based on quenching experiments and electron spin resonance (ESR)

analyses. Furthermore, density function theory (DFT) calculations were performed to investigate the active sites of these SACs, and the effect of P doping on the coordination environment of their Co atoms and their performance in PMS activation and SDZ degradation. The experimental and calculation results were considered to determine the effectiveness of heteroatoms, such as P, for regulating the coordination environment of Co sites in SACs, and whether the introduction of P atoms enhances the catalytic activity of Co-based SACs in PMS activation and organic pollutant degradation processes.

2. Materials and methods

2.1. Chemicals and materials

Zinc nitrate hexahydrate ($\text{Zn}(\text{NO}_3)_2 \cdot 6\text{H}_2\text{O}$, 99.99%), SDZ (99%), sulfamethazine (SMZ, 99%), ofloxacin (OFX, 98%), erythromycin (ERY, 98%), tetracycline (TET, 98%), oxytetracycline (OTET, 98%) and clindamycin (CLD, 98%) were obtained from Sigma-Aldrich (St. Louis, MO, USA). Cobaltous nitrate hexahydrate ($\text{Co}(\text{NO}_3)_2 \cdot 6\text{H}_2\text{O}$, 99%), 2-methylimidazole (2-Melm, 98%), triarylphosphine (TPP, 99%), Oxone® (potassium PMS), sodium hydroxide (NaOH, 97%), sodium thiosulfate ($\text{Na}_2\text{S}_2\text{O}_3$, 99%), sodium chloride (NaCl, 99.9%), sodium bicarbonate (NaHCO_3 , 99.8%), sodium nitrate (NaNO_3 , 99%), sodium dihydrogen phosphate (NaH_2PO_4 , 99.9%), methanol (MeOH, 99.9%), *tert*-butyl alcohol (TBA, 99.5%), 1,4-benzoquinone (*p*-BQ, 99%), and furfuryl alcohol (FFA, 98%) were purchased from Aladdin (Shanghai, China). Sodium azide (NaN_3 , 99%) was obtained from FuChen (Tianjin, China). 5,5-Dimethyl-1-pyrroline-*N*-oxide (DMPO) and 2,2,6,6-tetramethyl-4-piperidone hydrochloride (TEMP) were obtained from Dojindo (Kumamoto, Japan). Ultrapure water ($18.2 \text{ M}\Omega \text{ cm}^{-1}$) was produced using a Milli-Q system (Millipore, MA, USA).

2.2. Preparation of ZIF-based precursors

All ZIF precursors were prepared by rapidly adding Solution B to Solution A, followed by stirring at 300 rpm for 30 min at 25 °C.

ZIF-8: To form Solution A, 2.440 g of $\text{Zn}(\text{NO}_3)_2 \cdot 6\text{H}_2\text{O}$ was dissolved in 150 mL methanol with stirring at 300 rpm. To form Solution B, 3.080 g of 2-Melm was dissolved in 75 mL methanol with thorough stirring at 300 rpm.

ZIF-8-P: TPP was used as the precursor to encapsulate P in the ZIF-8 framework by doping P into the carbon matrix during pyrolysis [35]. To form Solution A, 2.440 g of $\text{Zn}(\text{NO}_3)_2 \cdot 6\text{H}_2\text{O}$ was dissolved in 150 mL methanol with stirring at 300 rpm. The resulting solution was treated with 1.875 g TPP, and stirring was continued until the TPP was completely dissolved. To form Solution B, 3.080 g of 2-Melm was dissolved in 75 mL methanol with thorough stirring at 300 rpm.

ZIF-8-Co: Co was encapsulated in the ZIF-8 framework to construct single-atom Co sites. To form Solution A, 2.440 g of $\text{Zn}(\text{NO}_3)_2 \cdot 6\text{H}_2\text{O}$ and 0.170 g of $\text{Co}(\text{NO}_3)_2 \cdot 6\text{H}_2\text{O}$ were dissolved in 150 mL methanol with stirring at 300 rpm. To form Solution B, 3.080 g of 2-Melm was dissolved in 75 mL methanol with thorough stirring at 300 rpm.

ZIF-8-Co/P: P was encapsulated with Co in the ZIF-8 framework to regulate the electronic structure and coordination environment of the Co sites [35]. To form Solution A, 2.440 g of $\text{Zn}(\text{NO}_3)_2 \cdot 6\text{H}_2\text{O}$ and 0.170 g of $\text{Co}(\text{NO}_3)_2 \cdot 6\text{H}_2\text{O}$ were dissolved in 150 mL methanol with stirring at 300 rpm. The resulting solution was treated with 1.875 g TPP, and stirring was continued until the TPP was completely dissolved. To form Solution B, 3.080 g of 2-Melm was dissolved in 75 mL methanol with thorough stirring at 300 rpm.

2.3. Preparation of ZIF-derived catalysts

The prepared ZIF-8-based precursors were processed to synthesise various ZIF-derived catalysts. Thus, the solution of a given precursor was transferred to four 100 mL Teflon-lined stainless-steel autoclaves, which

were then subjected to hydrothermal reaction conditions: i.e., heated at 120 °C in an oven for 4 h. After cooling to room temperature, the precipitates formed in the solutions were collected by centrifugation and washed with methanol three times. The resultant powder was vacuum dried at 70 °C for 10 h, and then pyrolysed in a tubular furnace at 950 °C for 3 h under a continuous flow of nitrogen [33,36]. Subsequently, the furnace was allowed to cool naturally, and the pyrolysed material (a black powder) was collected and ground. The pulverised powder was washed successively with water (50 mL) twice and methanol (50 mL) twice, and then vacuum dried at 60 °C for 10 h to obtain the catalyst product. The carbon-based catalysts prepared from various ZIF-8 precursors – ZIF-8, ZIF-8-P, ZIF-8-Co and ZIF-8-Co/P – were respectively labelled as ZIF-C, ZIF-P-C, ZIF-CoN₄-C and ZIF-CoN₃P-C. Together, as a group, they were named ZIF-derived catalysts, or ZIF-catalysts.

2.4. Characterisation of the ZIF-derived catalysts

Methods of characterisation of the catalyst materials are detailed in Text S1, [Supporting Information](#), including characterisations by X-ray diffraction (XRD), high-resolution transmission electron microscopy (HR-TEM), high-angle annular dark-field scanning transmission electron microscopy (HAADF-STEM), Fourier-transform infrared (FT-IR) spectrometer, X-ray photoelectron spectroscopy (XPS), inductively coupled plasma-optical emission spectrometry (ICP-OES), and inductively coupled plasma-mass spectrometry (ICP-MS).

2.5. Catalytic degradation of pollutants by PMS with the ZIF-derived catalysts

The activity of the ZIF-catalysts in PMS activation and persulfate-based AOPs was investigated with regard to the oxidation and degradation of SDZ (10 mg L⁻¹) in water at 20 ± 1 °C. Typically, 2.5 mg of the catalyst was dispersed in 50 mL of SDZ solution (which had been sonicated for 30 s) in a 100 mL glass beaker with continuous stirring. The resulting suspension was stirred for 10 min to ensure an SDZ-catalyst adsorption-desorption equilibrium was established. The AOP was initiated by adding 0.50 mL of a PMS stock solution (0.1 M), corresponding to a dosing concentration of 1 mM PMS. During the reaction, 0.9 mL aliquots of the suspension were removed at pre-determined time intervals. Each sample was rapidly mixed with 0.1 mL of Na₂S₂O₃ solution (0.1 M) to deplete the residual PMS, and the resulting mixture was filtered through a 0.45 µm PTFE membrane before analysis. The concentration of SDZ in the filtrate was determined by high-performance liquid chromatography (HPLC) (1260 Infinity II, Agilent, USA). Moreover, the SDZ degradation products were analysed through high-performance liquid chromatography-quadrupole time-of-flight mass spectrometry (HPLC-QTOF-MS) (Impact II™, Bruker, Germany).

2.6. Computational methods

Spin-polarised DFT calculations were performed using the Vienna ab initio simulation package (VASP, v.5.4.4) [37]. The exchange-correlation potentials were described by the generalised gradient approximation in the form of the Perdew-Burke-Ernzerhof functional. The ion-electron interactions were determined by considering the projector-augmented wave pseudopotential for the core electrons, with a cut-off energy of 500 eV for the valence electrons. The two-dimensional graphene support was modelled using a 6 × 6 supercell separated by a vacuum slab height of 15 Å, to avoid strong interactions between two adjacent layers. Sampling was performed from 2 × 2 × 1 and 6 × 6 × 1 k-point grids for the structural optimisations and electron density calculations, respectively. The convergence criteria for the electron self-consistent field and interaction were 0.02 eV/Å and 10⁻⁵ eV, respectively. Grimme's zero damping DFT-D3 method was used to incorporate the van der Waals interactions [38]. The adsorption energy for the PMS adsorption by the catalyst was estimated using Eq. (1):

$$E_{\text{ads}} = E_{\text{total}} - E_{\text{substrate}} - E_{\text{PMS}} \quad (1)$$

where E_{total} , $E_{\text{substrate}}$ and E_{PMS} represent the total energy of the adsorption system, the energy of the clean substrate and the energy of the free PMS molecule, respectively. The change in reaction energies (ΔE) for PMS catalysis was calculated based on the adsorption, activation and regeneration steps. The charge differential analysis was performed using Eq. (2):

$$\rho_{\text{diff}} = \rho_{\text{total}} - \rho_{\text{substrate}} - \rho_{\text{PMS}} \quad (2)$$

where ρ_{total} , $\rho_{\text{substrate}}$ and ρ_{PMS} denote the electron density of the adsorption system, the clean substrate and the free PMS molecule, respectively. The atomic charges were calculated using the atom-in molecule scheme proposed by Bader [39]. The electron localisation function (ELF) was computed to measure the electron localisation in ZIF-CoN₄-C and ZIF-CoN₃P-C [40]. The work function was analysed to reflect the electron escape ability at a ZIF-CoN₄-C surface with and without P doping [41].

3. Results and discussion

3.1. Characterisation of ZIF-derived catalysts

To investigate the PMS-activation enhancement associated with the P doping of the Co-SACs, it was necessary to maintain the overall structure of the ZIF-based catalysts prepared by the same pyrolysis strategy, i.e., ZIF-C, ZIF-P-C, ZIF-CoN₄-C and ZIF-CoN₃P-C. XRD analysis was conducted to clarify the crystallographic phases of these catalysts. As shown in Fig. S1a, the four catalysts share similar patterns, and no Co-containing crystalline particles are observed. Amorphous carbon is the main phase in the ZIF-based materials. The broad peaks occurring at 25° and 44° correspond to the (0 0 2) and (1 0 1) phases in graphite, respectively. The Raman spectra, shown in Fig. S1b, indicate three peaks, consistent with the D band (1342 cm⁻¹), G band (1578 cm⁻¹) and 2D band (2800 cm⁻¹), respectively. In general, the D band represents defect-induced features; the G band indicates the graphitisation degree of carbon [42]; and the 2D band is considered the overtone of the D band and is associated with the stacking order of the graphitic structure in one direction [43]. The ratio of the intensity of the D band to the intensity of the G band (I_D/I_G) for each of the four ZIF-derived catalysts (Fig. S1b) are similar, indicating that the catalysts share a similar carbon skeleton. The magnitude of I_D/I_G height ratio slightly increased (from 1.09 to 1.13) for ZIF-CoN₄-C and ZIF-CoN₃P-C, indicating the diminution of the sp² domains in these two catalysts [44]. The FT-IR spectra of the ZIF-catalysts have peaks in the area from 1000 to 1300 cm⁻¹, corresponding to C–O or C–N stretching vibrations (Fig. S1c) [45]. Another broad peak is present in the range from 1450 to 1600 cm⁻¹, and is attributable to a symmetric C=O or C=N stretching vibration [46].

The performance of these catalysts is influenced by their surface area and pore structure, which may affect the mass transport rate [47]. The specific surface areas of ZIF-C, ZIF-P-C, ZIF-CoN₄-C and ZIF-CoN₃P-C were found to be 770.41, 817.47, 737.24 and 744.64 m² g⁻¹, respectively (Fig. S1d). As indicated in Table S1, the pore volume and average pore size were similar in the four ZIF-derived catalysts. As shown in Fig. S2, the hierarchically porous architecture would promote the mass transport during the catalytic process [36]. In general, the ZIF-catalysts shared a similar porous structure and channel environment. Moreover, according to the XRD, Raman, FT-IR and surface area analyses, the introduction of Co and P did not considerably change the inherent framework and porous structure of the ZIF-catalysts.

ZIF-CoN₃P-C was prepared by in situ doping of TPP molecules into the ZIF-8 framework, such that Co²⁺ replaced the Zn²⁺ nodes and coordinated with 2-MeIm (Fig. 1a). According to the HR-TEM images of ZIF-CoN₃P-C (Fig. 1b), the structural features of hexagonal ZIF-8 were retained after pyrolysis, and the resulting ZIF-CoN₃P-C sized

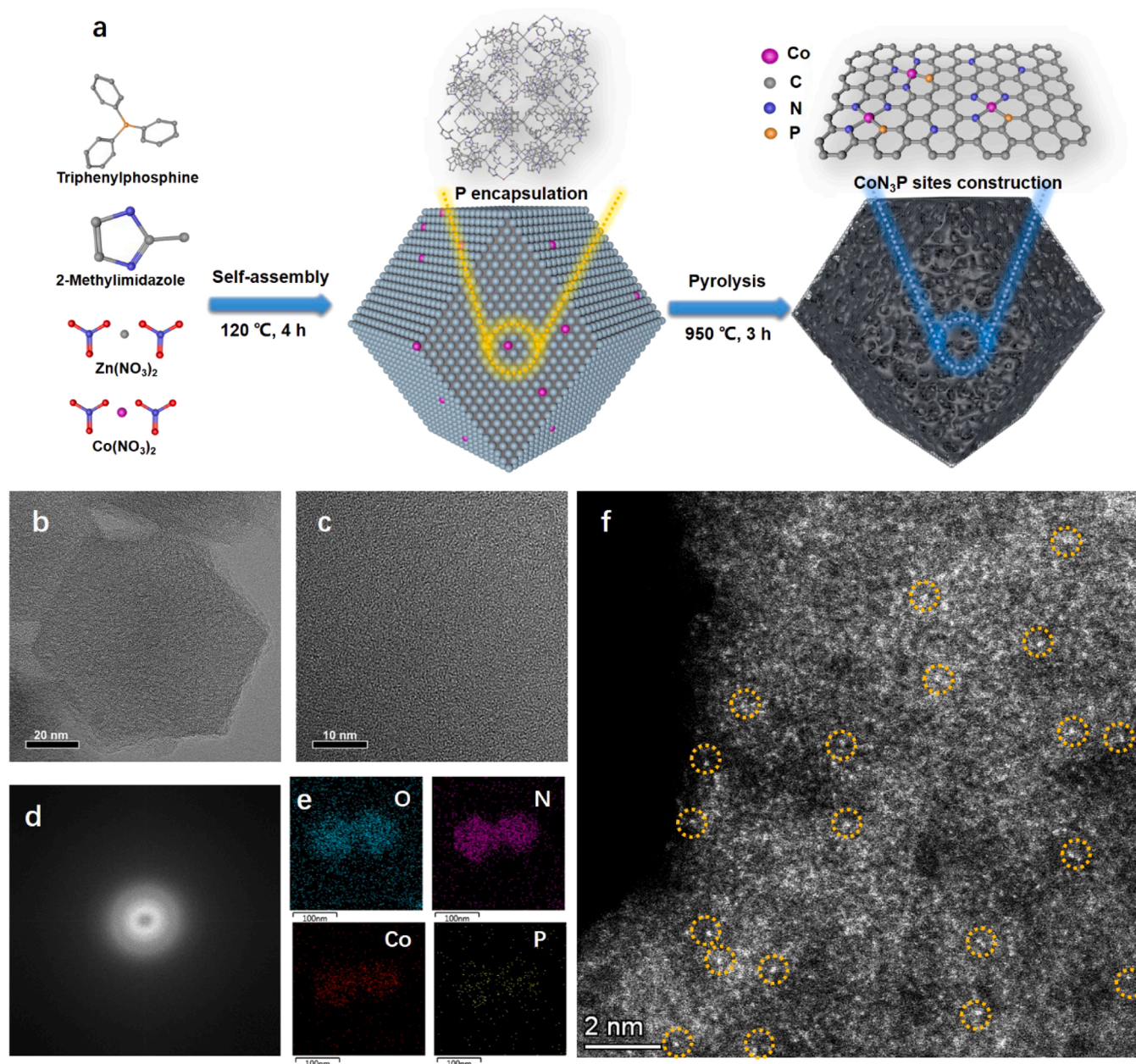


Fig. 1. Synthesis and morphology of the ZIF- $\text{CoN}_3\text{P-C}$ catalyst: (a) synthesis procedure, (b) HR-TEM image, (c) magnified HR-TEM image, (d) ring-like selected area electron diffraction (SEAD) pattern, (e) EDS maps and (f) HAADF-STEM.

approximately 100 nm. The distribution of amorphous carbon was randomly uniform, and the ring-like selected-area electron diffraction patterns confirms the low crystallinity of ZIF- $\text{CoN}_3\text{P-C}$ (Fig. 1c and d). No Co-containing clusters are observed, consistent with the XRD result. Elemental mapping by energy-dispersive X-ray spectroscopy (EDS) indicates the homogeneous distributions of elements N, O and Co on ZIF- $\text{CoN}_3\text{P-C}$ (Fig. 1e). Elemental P was detected in a low concentration, owing to its relatively low abundance in ZIF- $\text{CoN}_3\text{P-C}$. From the HAADF-STEM image, several isolated bright dots (marked with orange circles in Fig. 1f) indicate the Co atoms on the carbon support.

The XPS results were examined to identify the constituent elements and chemical states in the different ZIF-catalysts (Fig. 2 and S3–S4). The XPS spectra confirm the presence of C, N and O elements in all ZIF-catalysts. The atomic percentages of C, N, O, Co and P are listed in Table S2. The high-resolution C 1s XPS spectra of ZIF- $\text{CoN}_4\text{-C}$ and ZIF- $\text{CoN}_3\text{P-C}$ indicate the presence of four C species: $\text{C}=\text{C}$ (284.8 eV), $\text{C}-\text{N}$ (286.3 eV), $\text{C}=\text{O}$ (287.8 eV) and $\text{O}-\text{C}=\text{O}$ (290.0 eV) (Fig. 2a) [48]. The

strong $\text{C}=\text{C}$ bond in ZIF-catalysts is attributable to the graphene matrix, which has been noted to enhance electron transfer, and could thus promote PMS activation [49]. The N 1s spectrum can be deconvoluted into five types of N species: pyridinic N, pyrrolic N, graphitic N, oxidised N and a $\text{Co}-\text{N}$ bond (Fig. 2b). The highest proportion corresponds to pyridinic N, which provides the coordination sites for metallic species and stabilised the metal atoms [50]. Compared with ZIF- $\text{CoN}_4\text{-C}$, the P 2p spectrum of ZIF- $\text{CoN}_3\text{P-C}$ indicates the presence of two peaks at binding energies of 132.5 eV and 133.5 eV, corresponding to the $\text{P}-\text{C}$ and $\text{P}-\text{N}$ bonds, respectively (Fig. 2c) [51]. The P doping likely altered the electronic structure of the catalyst, which would facilitate its electron transfer to PMS molecules. The findings shown in Fig. 2d confirm the presence of only Co(II) species (780.8 eV) on the surface of ZIF- $\text{CoN}_4\text{-C}$ and ZIF- $\text{CoN}_3\text{P-C}$. The Co loading determined by the ICP-OES analysis is 1.68 wt% and 1.65 wt% for ZIF- $\text{CoN}_4\text{-C}$ and ZIF- $\text{CoN}_3\text{P-C}$, respectively (Table S2). Overall, the ZIF-derived catalysts exhibit a similar carbon matrix and nitrogen-rich support (Figs. S3–S4). The

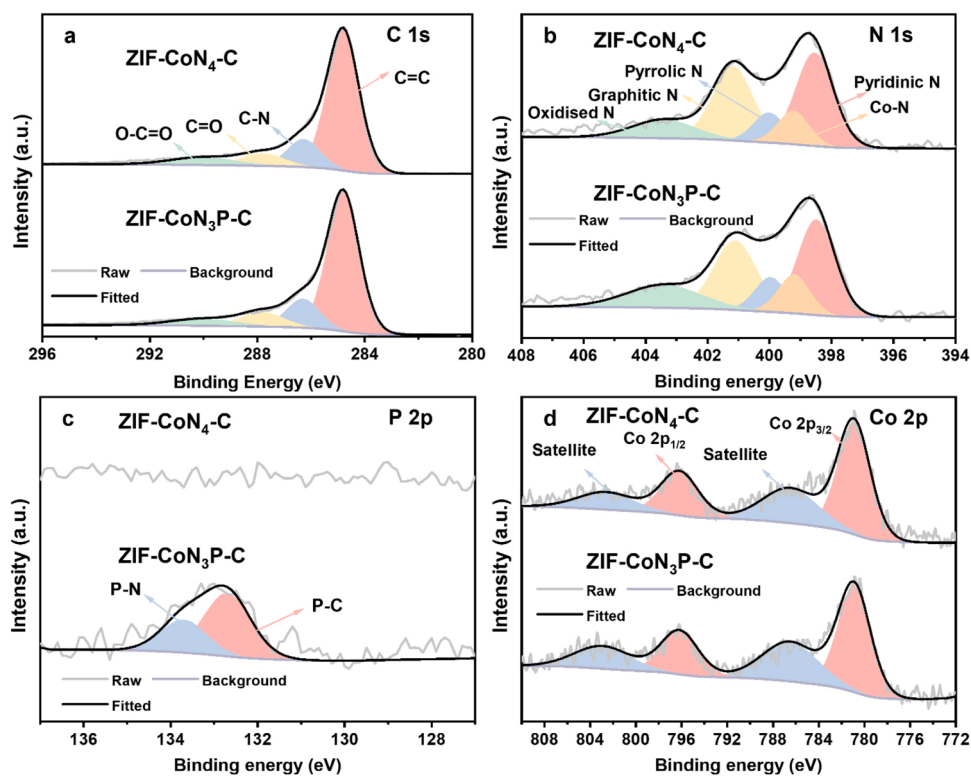


Fig. 2. High-resolution XPS spectra of (a) C 1s, (b) N 1s, (c) P 2p and (d) Co 2p for ZIF-CoN₄-C and ZIF-CoN₃P-C.

introduction of elemental Co and P did not lead to notable macroscopic variations between the different catalysts, except for the presence of Co and P altering the coordination environment of single-atom Co sites on

the catalysts.

X-ray absorption near-edge structure (XANES) and extended X-ray absorption fine structure (EXAFS) analyses were performed to gain

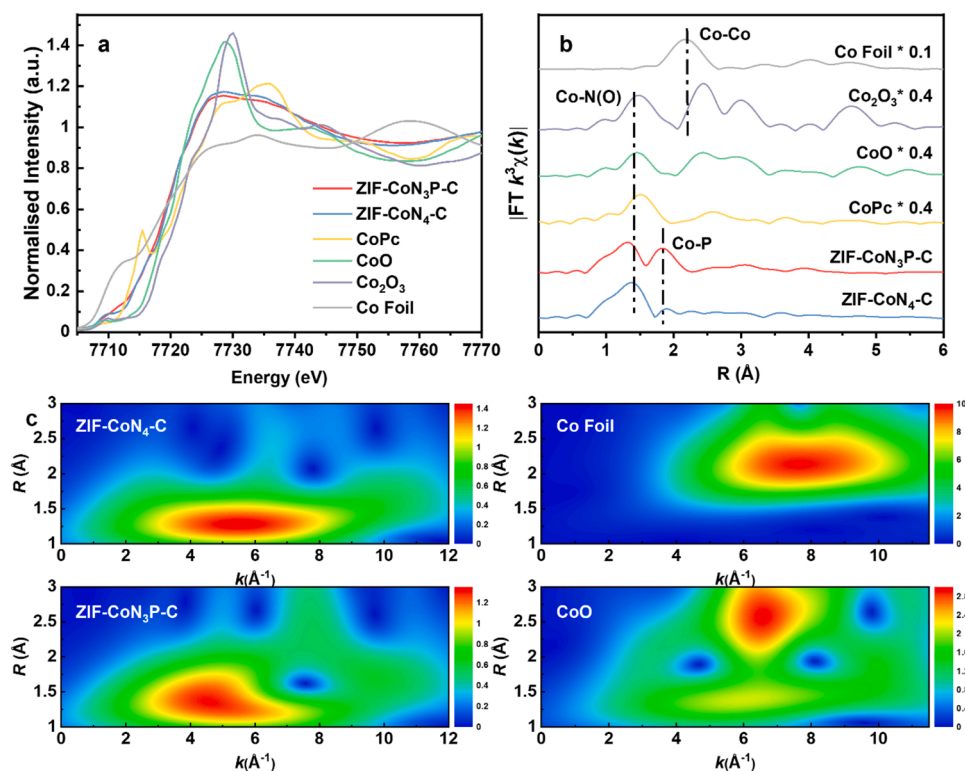


Fig. 3. Investigation of the chemical state and coordination environment of the Co sites in ZIF-CoN₄-C and ZIF-CoN₃P-C: (a) normalised XANES spectra at the Co K-edge of ZIF-CoN₄-C, ZIF-CoN₃P-C, Co foil, Co₂O₃, CoO and CoPc; (b) FT magnitude of the experimental EXAFS spectra of ZIF-CoN₄-C, ZIF-CoN₃P-C, with those of Co foil, Co₂O₃, CoO and CoPc presented as references; and (c) wavelet transform plots of the Co K-edge.

insights into the single-atom Co sites at the atomic level. The normalised Co K-edge XANES spectra of ZIF-CoN₄-C and ZIF-CoN₃P-C were compared with reference spectra of Co foil, cobalt(III) oxide (Co₂O₃), cobalt(II) oxide (CoO) and cobalt phthalocyanine (CoPc) (Fig. 3a). The absorption edges of ZIF-CoN₄-C and ZIF-CoN₃P-C at the normalised intensity of 0.5 are located close to that of CoO, indicating that the chemical states of Co are nearly that of Co(II). The FT-EXAFS spectra of ZIF-CoN₄-C, ZIF-CoN₃P-C and other references (Co foil, Co₂O₃, CoO and CoPc) are shown in Fig. 3b. FT peaks of ZIF-CoN₄-C and ZIF-CoN₃P-C are located at 1.34 Å and 1.40 Å, which are attributable to the scattering of Co–N coordination. Moreover, a weaker FT peak at 1.84 Å is seen in ZIF-CoN₃P-C, which likely results from the Co–P scattering. Furthermore, no FT peaks corresponding to Co–Co coordination are detected. The characteristic results of EXAFS and STEM analyses confirm that the Co single-atom sites were well constructed. To further investigate the coordination environment of Co with the P doping, the Artemis module was formulated to fit the FT-EXAFS curves, and the fitting parameters are listed in Table S3 (Fig. S5). The results reveal that the coordination numbers of Co–N and Co–P in ZIF-CoN₃P-C are 2.8 and 0.9 with the average bond length of 1.856 Å and 2.253 Å, respectively, which differ greatly from the coordination number of Co–N (4.1) in ZIF-CoN₄-C (Table S3). The wavelet transform (WT) technique was used to examine the atomic mono-dispersity, considering the strong resolution between the k and R spaces [52]. The WT plots of ZIF-CoN₄-C, ZIF-CoN₃P-C, Co foil and CoO are shown in Fig. 3c. According to the WT plots, the intensity maxima occurs at 5.43 Å⁻¹ for ZIF-CoN₄-C and 4.85 Å⁻¹ for ZIF-CoN₃P-C, which are attributable to their different Co–N coordination [53]. These values are significantly different from those of Co foil (7.83 Å⁻¹) and CoO (6.72 Å⁻¹). Overall, the above results confirm that the cobalt atoms are atomically dispersed while the CoN₄ and CoN₃P sites are indeed constructed distinctly.

3.2. Enhanced catalytic performance of the ZIF-CoN₃P-C catalyst

SDZ was used as the model pollutant to evaluate the catalytic activity of ZIF-CoN₃P-C. The adsorption experiment results indicate that there was negligible adsorption of SDZ by the ZIF-derived catalysts (Fig. S6). Based on the adsorption results, SDZ oxidation tests were initiated after 10 min of adsorption. As depicted in Fig. 4a, in the presence of PMS and no catalysts, only a slight degradation of SDZ occurred, owing to the low oxidation potential of PMS ($E_0 = 1.82$ V). When ZIF-C and ZIF-P-C were added as the catalysts, the SDZ degradation efficiencies were found to be 17.9% and 20.7%, respectively, with pseudo-second-order reaction rates of 0.006×10^5 and 0.007×10^5 M⁻¹ min⁻¹, respectively, which are slightly higher than that for only PMS (0.004×10^5 M⁻¹ min⁻¹) (Text S2). The SDZ degradation results indicate that the ZIF-C carbon support without Co atoms could not effectively activate the PMS. However, when single Co atoms were introduced into the ZIF-C catalyst, the SDZ degradation efficiency significantly increased to 96.9% within 10 min. This finding verifies the remarkable reactivity of ZIF-CoN₄-C as a catalyst for PMS activation. In the same experimental conditions, the SDZ degradation rate constant of ZIF-CoN₃P-C/PMS (1.074×10^5 M⁻¹ min⁻¹) was more than 2.5 times that of ZIF-CoN₄-C/PMS (0.420×10^5 M⁻¹ min⁻¹) (Fig. 4b). Compared to other Co-based catalysts reported in the literature, ZIF-CoN₃P-C exhibited a generally lower dosage and shorter half time (0.23 min), showing its high catalytic capacity for PMS activation and SDZ degradation (Table S4).

The effects of catalyst dosage and PMS concentration on the SDZ-oxidation performance of the ZIF-CoN₃P-C/PMS system were evaluated. As shown in Fig. 4c, the SDZ removal rate constant increased from 0.416 to 1.074, 2.391 and 2.522×10^5 M⁻¹ min⁻¹ as the ZIF-CoN₃P-C dosage was increased from 0.025 to 0.050, 0.075 and 0.100 g L⁻¹, respectively. A larger amount of PMS addition was expected to increase the opportunities for PMS to contact the active sites of the catalyst, and thus enhance the activation of PMS. As shown in Fig. 4d, an increase in the PMS dosing concentration (from 0.25 mM to 0.50 mM) considerably

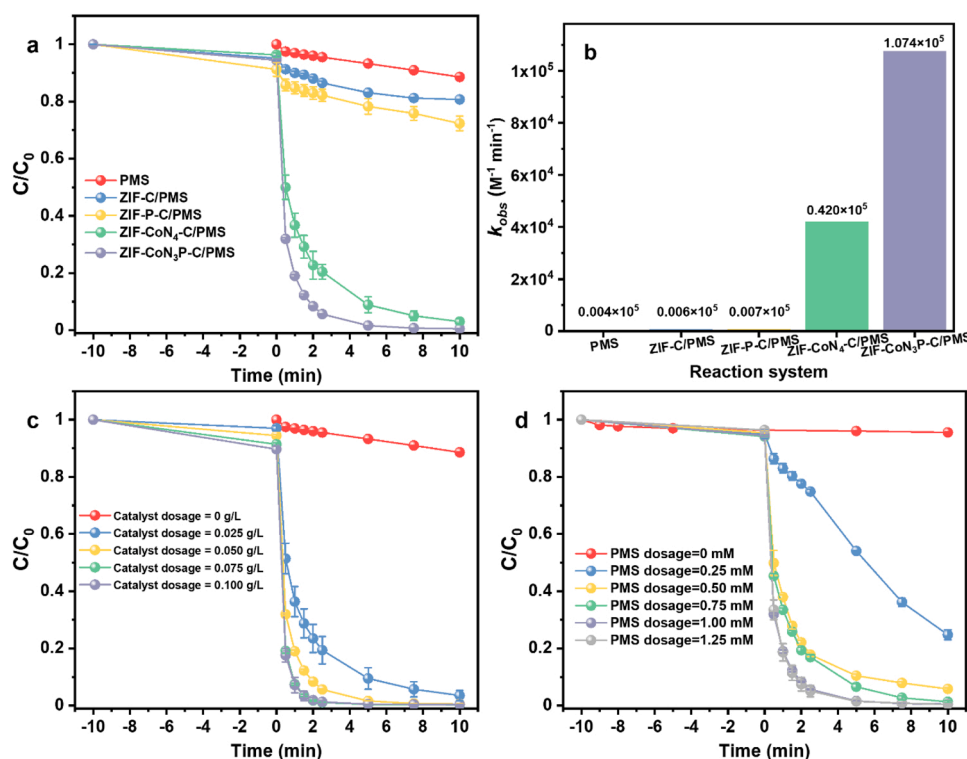


Fig. 4. Degradation of SDZ by PMS in different catalytic conditions: (a) removal efficiency and (b) corresponding degradation rate constants of SDZ in the presence of various catalysts for 10 min. Factors influencing the SDZ removal efficiency in the ZIF-CoN₃P-C/PMS system: (c) catalyst dosage and (d) PMS dosage. Reaction conditions: [SDZ] = 10 mg L⁻¹, [catalyst] = 0.050 g L⁻¹ for (a) and (d), [PMS] = 1 mM for (a) and (c), reaction pH = 3.35 ± 0.1, temperature = 20 ± 1 °C.

increased the SDZ degradation efficiency from 75.2% to 94.1%.

3.3. Identification of predominant ROS

Quenching experiments were conducted to investigate the dominant ROS in the ZIF- $\text{CoN}_3\text{P-C/PMS}$ system. MeOH was used as the quenching agent for hydroxide and sulphate radicals ($\cdot\text{OH}$ and $\text{SO}_4^{\cdot-}$) with rate constants of $9.7 \times 10^8 \text{ M}^{-1} \text{ s}^{-1}$ and $1.6\text{--}7.7 \times 10^7 \text{ M}^{-1} \text{ s}^{-1}$, respectively [54]. The SDZ degradation efficiency did not decrease, and 99.4% of the SDZ could still be removed in 10 min, even when the MeOH:PMS ratio was increased to 500:1 (Fig. 5a). TBA was used as another radical quenching agent, which has a higher affinity for $\cdot\text{OH}$ ($(3.8\text{--}7.6) \times 10^8 \text{ M}^{-1} \text{ s}^{-1}$) than $\text{SO}_4^{\cdot-}$ ($(4.0\text{--}9.1) \times 10^5 \text{ M}^{-1} \text{ s}^{-1}$) [55]. Similar results were obtained: the quenching effect of TBA on SDZ degradation was minor when the TBA:PMS ratio increased from 50:1–500:1 (Fig. 5b). The results indicate that $\cdot\text{OH}$ and $\text{SO}_4^{\cdot-}$ radicals were not the primary ROS in the ZIF- $\text{CoN}_3\text{P-C/PMS}$ system. Considering that $^1\text{O}_2$ could be formed when the Co- N_4 structure was involved in PMS activation, NaN_3 and FFA were used as the $^1\text{O}_2$ probes [34]. As shown in Fig. 5c, the SDZ oxidation was significantly hindered, and the degradation efficiency

decreased from 99.5% to 30.0% for the NaN_3 :PMS ratio of 20:1. The reaction rate constant decreased from 1.074×10^5 to 0.044×10^5 , 0.036×10^5 , 0.018×10^5 and $0.017 \times 10^5 \text{ M}^{-1} \text{ min}^{-1}$ when the NaN_3 :PMS ratio increased to 5:1, 10:1, 15:1 and 20:1, respectively. Besides, FFA also effectively decreased the SDZ degradation efficiency, and the corresponding rate constant decreased from 0.054×10^5 to $0.011 \times 10^5 \text{ M}^{-1} \text{ min}^{-1}$ when the FFA:PMS ratio increased from 50 mM to 500 mM (Fig. S7a). These quenching results indicate that $^1\text{O}_2$, rather than other radicals, was the dominant ROS produced from PMS by ZIF- $\text{CoN}_3\text{P-C}$.

In the context of transition-metal-based PMS activation, high-valent metallic species were expected to contribute to the enhanced organic degradation efficacy [56]. To examine the generation of high-valent Co-oxo species (Co(III) and Co(IV)), dimethyl sulphoxide (DMSO), which can reduce a high-valent Co-oxo species to Co(II) with a rate constant of $2.4 \times 10^6 \text{ M}^{-1} \text{ s}^{-1}$, was used as the probing agent [56]. Excessive DMSO addition (DMSO/PMS ratios from 5:1–50:1) did not prominently hinder the SDZ degradation (Fig. 5d). According to the different quenching tests on SDZ degradation, $^1\text{O}_2$ was the dominant ROS in the ZIF- $\text{CoN}_3\text{P-C/PMS}$ system.

To identify the ROS more directly, DMPO was used as the spin-

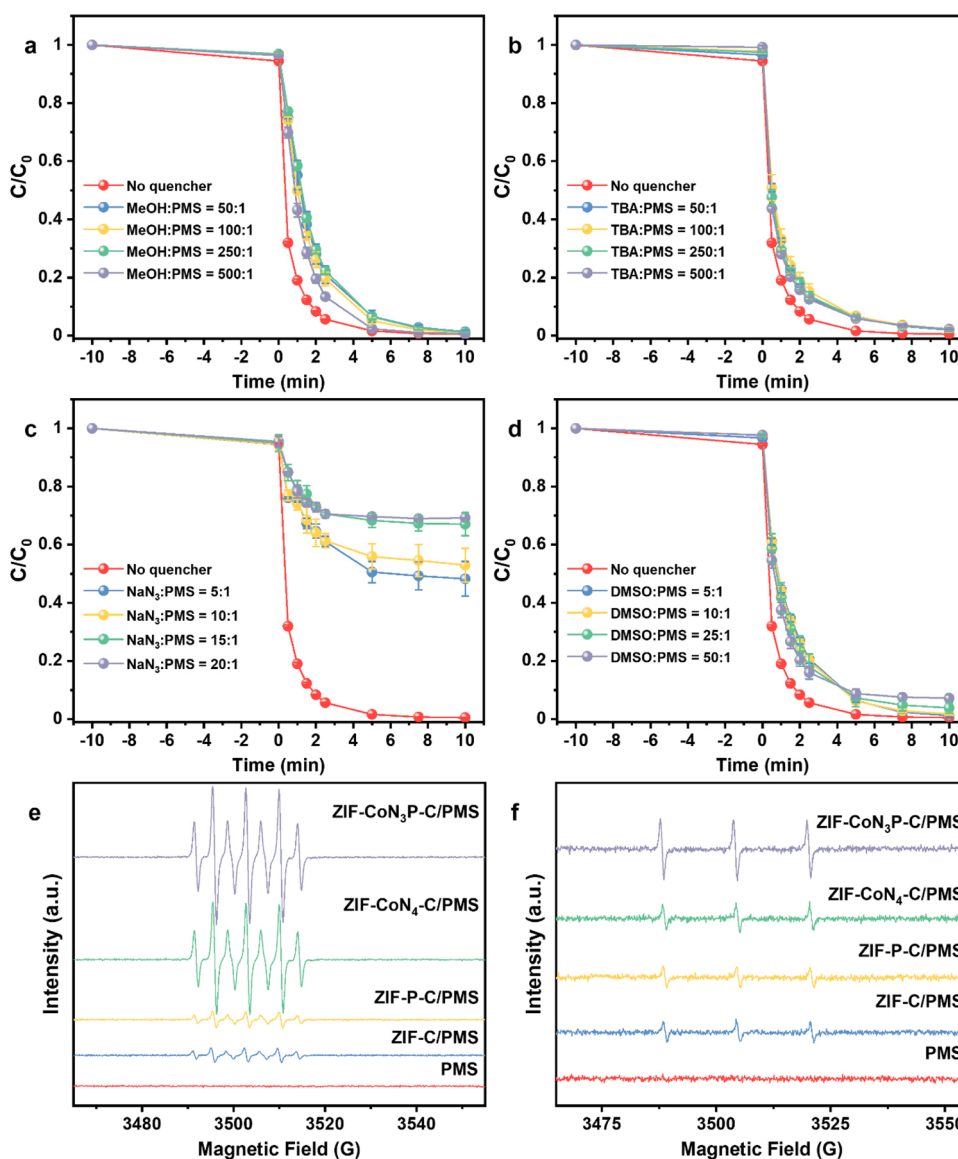
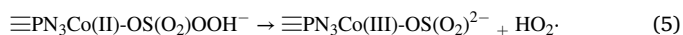
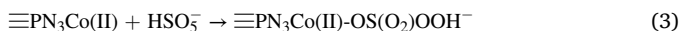


Fig. 5. Effects of the ROS quenching agents on SDZ degradation in the ZIF- $\text{CoN}_3\text{P-C/PMS}$ system: (a) MeOH, (b) TBA, (c) NaN_3 and (d) DMSO, (e) DMPO-trapped and (f) TEMP-trapped ESR spectra for the activation of PMS by ZIF- $\text{CoN}_3\text{P-C}$. Reaction conditions: [SDZ] = 10 mg L^{-1} , [catalyst] = 0.050 g L^{-1} , [PMS] = 1 mM , reaction pH = 3.35 ± 0.1 , temperature = $20 \pm 1 \text{ }^\circ\text{C}$.

trapping agent in ESR to detect the dominant ROS generated by the various ZIF-catalysts. As depicted in Fig. 5e, the ESR spectrum with only PMS does not exhibit any characteristic peak, indicating that no radicals were generated when PMS directly reacted with SDZ. Upon the addition of ZIF-catalysts, the formation of 5,5-dimethyl-2-pyrrolidone-N-oxyl (DMPOX) was detected, which is attributable to the oxidation of DMPO. In the ESR analysis, the DMPOX signals appear as seven peaks in an intensity ratio of 1:2:1:2:1:2:1 and the hyperfine coupling constants of $\alpha_N = 3.8$ G and $\alpha_H = 7.3$ G are consistent with that of DMPOX. Diverse causes have been reported for the generation of DMPOX; in particular, the presence or absence of radicals could both result in the formation of DMPOX [57]. Specifically, DMPO–OH could be transformed to DMPOX with excessive oxidation by $\cdot\text{OH}$ and $\text{SO}_4^{\cdot-}$. Meanwhile, the $^1\text{O}_2$ -mediated non-radical activation would contribute to the DMPOX signal [58]. DMPO can react with $^1\text{O}_2$ to generate the DMPO–OH adduct, followed by the formation of a DMPO nitronium cation, leading to DMPOX signals [59].

Because the ROS species could not be conclusively identified with the DMPO trapping when DMPOX was detected, TEMP was used as the trapping agent to confirm the presence of $^1\text{O}_2$ [60]. In contrast to the case of the sole PMS system without catalysts, three peaks with peak intensities of 1:1:1 ($\alpha_N = 15.8$ G) were detected for $^1\text{O}_2$ in the ESR of the ZIF-catalyst/PMS systems (Fig. 5f). The peak intensity for ZIF- $\text{CoN}_3\text{P-C}$ was considerably higher than those of the other ZIF-catalysts, apparently because of the higher $^1\text{O}_2$ concentration in the liquid phase. After clarifying the dominant role of $^1\text{O}_2$ in the ZIF- $\text{CoN}_3\text{P-C}$ /PMS system, the $^1\text{O}_2$ generation process was further investigated. *p*-BQ, a typical quenching agent of $\text{HO}_2\cdot/\text{O}_2^{\cdot-}$, ranging from 5 mM to 20 mM could inhibit about 50% of the SDZ degradation efficiency (Fig. S7b). The $\text{HO}_2\cdot/\text{O}_2^{\cdot-}$ is considered as the key intermediate for the $^1\text{O}_2$ formation, and the recombining rate of $\text{HO}_2\cdot/\text{O}_2^{\cdot-}$ ($9.7 \times 10^7 \text{ M}^{-1} \text{ s}^{-1}$) is much faster than the rate of reactions between $\text{HO}_2\cdot/\text{O}_2^{\cdot-}$ and electron-rich organics [33,61]. Considering that NaN_3 could not quench the $\text{HO}_2\cdot/\text{O}_2^{\cdot-}$ -dominated reaction and no signal of $\text{HO}_2\cdot/\text{O}_2^{\cdot-}$ was detected by ESR test, $\text{HO}_2\cdot/\text{O}_2^{\cdot-}$ was only the intermediate of $^1\text{O}_2$ generation [61,62]. Thus, based on the above analysis, the pathway of $^1\text{O}_2$ generation may be proposed. Firstly, the dissociated PMS molecule (HSO_5^-) is chemically adsorbed on the CoN_3P site ($\equiv\text{PN}_3\text{Co}$) (Eq. (3)). Secondly, an electron transfers from $\equiv\text{PN}_3\text{Co(II)}$ to the adsorbed HSO_5^- , generating $\text{HO}_2\cdot$ and $\text{O}_2^{\cdot-}$ (Eqs. (4) and (5)), and $\text{O}_2^{\cdot-}$ can be protonated ($\text{pK}(\text{HO}_2\cdot/\text{O}_2^{\cdot-}) = 4.7$) (Eq. (6)). Thirdly, recombination of $\text{HO}_2\cdot$ and $\text{O}_2^{\cdot-}$ occurs to produce $^1\text{O}_2$ (Eqs. (7) and (8)).



3.4. Mechanism of enhanced $^1\text{O}_2$ generation from PMS by ZIF- $\text{CoN}_3\text{P-C}$

To investigate the effect of the introduced P atoms on the catalytic activity of the Co-SACs at the atomic level, DFT calculations were performed to compare the ZIF- $\text{CoN}_4\text{-C}$ and ZIF- $\text{CoN}_3\text{P-C}$ catalysts. For simplicity, monolayer graphene was used as the carbon support [53], and the optimised structures are shown in Fig. S8a and b. In general, the electron density considerably influences the electron-accepting or electron-donating tendency [63]. For the ZIF-derived catalysts, the electron densities were characterised by constructing two-dimensional valence-electron density colour-filled maps. As shown in Fig. 6a and c, the Co atom occupies the region with the highest electron density, which is significantly higher than the densities around the Co atom. Furthermore, the ELF was determined, while a lower ELF indicates a higher tendency of delocalisation of electrons [40]. The Co atom was bounded by the ELF = 0 isosurface, which indicates that the electrons around the Co atom are especially prone to delocalisation (Fig. 6b). These findings suggested that Co atoms were the most active site. After the substitution of one N atom with one P atom, the electron density and electron delocalisation are further concentrated around the Co site instead of the introduced P site, implying that the Co active centre was not altered by the introduction of P atoms (Fig. 6c and d).

As the electronegativity of elemental P (2.19) is less than that of elemental N (3.09), a P atom can more easily donate its outer electron to the neighbouring Co atom. Bader charge analyses were conducted to quantify the redistribution of charge from ZIF- $\text{CoN}_4\text{-C}$ to ZIF- $\text{CoN}_3\text{P-C}$ after P doping. The results showed the Bader charge of Co is 0.89 e and 0.58 e in ZIF- $\text{CoN}_4\text{-C}$ and ZIF- $\text{CoN}_3\text{P-C}$, respectively (Table S5). The decreased charge of Co in ZIF- $\text{CoN}_3\text{P-C}$ indicates the shift of electrons from P to Co. Moreover, the work function was calculated to clarify the thermodynamic work required to extract electrons from the Fermi level to the surface vacuum level. The presence of P decreased the work function from 4.99 eV (ZIF- $\text{CoN}_4\text{-C}$) to 4.29 eV (ZIF- $\text{CoN}_3\text{P-C}$), which confirmed the occurrence of enhanced electron delocalisation in ZIF- $\text{CoN}_3\text{P-C}$ (Table S6). Hence, the introduction of the P heteroatom significantly enhanced the electron delocalisation of the Co atom in the

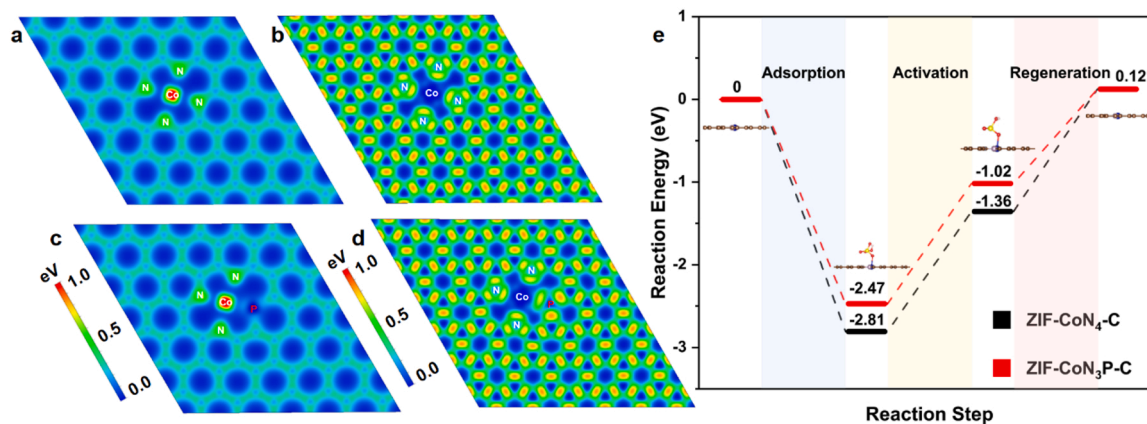


Fig. 6. DFT calculation of the electronic structure around the Co centre of the catalysts with and without P doping: electron density distributions of (a) ZIF- $\text{CoN}_4\text{-C}$ and (c) ZIF- $\text{CoN}_3\text{P-C}$; electron localisation functions of (b) ZIF- $\text{CoN}_4\text{-C}$ and (d) ZIF- $\text{CoN}_3\text{P-C}$; and (e) reaction energy of the steps of catalytic PMS activation on the surfaces of ZIF- $\text{CoN}_3\text{P-C}$ and ZIF- $\text{CoN}_4\text{-C}$.

catalyst.

Furthermore, the interaction between the Co atom and PMS molecules was investigated through theoretical calculations and experiment results. First, the PMS molecules were adsorbed on the Co site, and the adsorption configuration was optimised. The adsorption energy (E_{ads}) of PMS on Co in ZIF- $\text{CoN}_3\text{P-C}$ is -2.47 eV, whereas a smaller value of -2.81 eV is observed for ZIF- $\text{CoN}_4\text{-C}$. Generally, a more negative adsorption energy indicates a stronger adsorption of the PMS molecule. However, the strong binding of PMS-active sites may poison the sites, thereby weakening the desorption process [58]. The charge density analysis results indicate the potential electron transfer between the PMS molecule and Co site. Fig. S9a–d show the calculated charge-density difference before and after the introduction of P atoms in ZIF- $\text{CoN}_4\text{-C}$. The electrons accumulate around the PMS molecule instead of the Co atom, indicating that the electrons originally located around Co are transferred to the PMS molecule. In addition, the Bader charge of O in PMS in the initial and adsorbed states was calculated; this shows that approximately 0.77 electrons were transferred from Co to O of PMS through the formation of the Co–O bond (Table S5). Moreover, the reaction-free energy was calculated for the catalytic PMS activation process, including adsorption, activation and regeneration. In the PMS regeneration step shown in Fig. 6e, ZIF- $\text{CoN}_3\text{P-C}$ had a lower energy barrier (1.14 eV) than ZIF- $\text{CoN}_4\text{-C}$ (1.48 eV). Thus, the introduction of P favourably weakened the PMS adsorption and promoted the PMS regeneration. Overall, the induction of P and construction of CoN_3P enhanced the activity of ZIF- $\text{CoN}_3\text{P-C}$ for PMS activation.

3.5. Degradation pathway of SDZ in a ZIF- $\text{CoN}_3\text{P-C}$ /PMS system

According to the detected intermediates in the ZIF- $\text{CoN}_3\text{P-C}$ /PMS/SDZ system and the MS/MS spectra presented in Figs. S10–S12, three degradation pathways are proposed, as shown in Fig. 7. Pathway 1 is initiated by the oxidation of the phenylamino group, which generated the m/z 280.0208 intermediate. Multipoint degrees of hydroxylation occur on the aniline ring, with the formation of m/z 267.0381 and m/z 299.0110. The pyrimidine ring is cleaved to form the m/z 273.2703 intermediate, which transforms to the m/z 245.2390 intermediate. In Pathway 2, corresponding to the protonated form, m/z 186.0966 was detected in the first sample collected at 30 s. This detection confirms the occurrence of the Smiles rearrangement, which is attributable to the extrusion of sulphur(II) oxide from the SDZ molecule [64].

Based on the identification of the intermediates, the reaction sites on SDZ could be clarified, thereby validating the ROS generation. Compared to the ground state oxygen, $^1\text{O}_2$ in the excited state exhibits an empty $\pi^* 2p$ orbital, which could interact with a lone electron pair. During the oxidation of SDZ by $^1\text{O}_2$, single-electron transfer from the aniline ring or pyrimidine ring to $^1\text{O}_2$ was expected to occur. When the aniline moiety is initially oxidised by $^1\text{O}_2$, the intermediate radical cation of SDZ is formed. The subsequent oxidation of m/z 186.0966 could occur over the aniline ring, owing to the hydroxylation of the aniline group and formation of m/z 202.0916, m/z 216.0720 and m/z 187.0819. The detection of azo-intermediates indicated that dimerisation reactions occur between SDZ and its intermediates (Pathway 3). Therefore, the aromatic azoxy bond was likely produced by the nitroso and hydroxylamine building blocks with the participation of $^1\text{O}_2$ [65]. With continuous oxidation, these intermediates further decomposed to the final oxidation products, including nitrogen-containing ions, sulphate ions and aliphatic acids.

3.6. Stability and universality of ZIF- $\text{CoN}_3\text{P-C}$

Recycling tests were conducted to assess the stability and reusability of ZIF- $\text{CoN}_3\text{P-C}$ for the PMS-based AOP. As shown in Fig. 8a, the catalyst retained its catalytic performance after five test cycles, and more than 80% SDZ was degraded under the same reaction conditions. For the first three recycling tests, a total organic carbon removal efficiency of approximately 30% could be maintained (Fig. S13). The used catalyst did not adsorb a significant amount of SDZ in the cycling tests (Fig. 8a), likely because of the adsorbed organic products on the catalyst surface. In addition to the catalytic activity, the leaching and dissolution of Co ions from the catalyst were evaluated in different cycles (Fig. S14). After the 30 min reaction in the first cycle, $87.9 \mu\text{g L}^{-1}$ of Co ions was detected when 50 mg L^{-1} of ZIF- $\text{CoN}_3\text{P-C}$ was dosed. The Co leaching gradually declined from 72.5 to as low as $9.8 \mu\text{g L}^{-1}$ from the second to the fifth cycles. Furthermore, to investigate the possible changes of the coordination environment in ZIF- $\text{CoN}_3\text{P-C}$, samples used after for 3 and 5 cycles were characterised. As shown in Fig. S15, there is nearly no energy shift in the edge of XANES, indicating the stable chemical state of the Co centre. The coordination numbers of the fresh and used ZIF- $\text{CoN}_3\text{P-C}$ were all 2.8, and Co-P in ZIF- $\text{CoN}_3\text{P-C}$ (3 cycles) and ZIF- $\text{CoN}_3\text{P-C}$ (5 cycles) were both 1.0, similar to that of the fresh ZIF- $\text{CoN}_3\text{P-C}$ (0.9) (Table S3, Fig. S16). These results confirmed that the coordinated Co

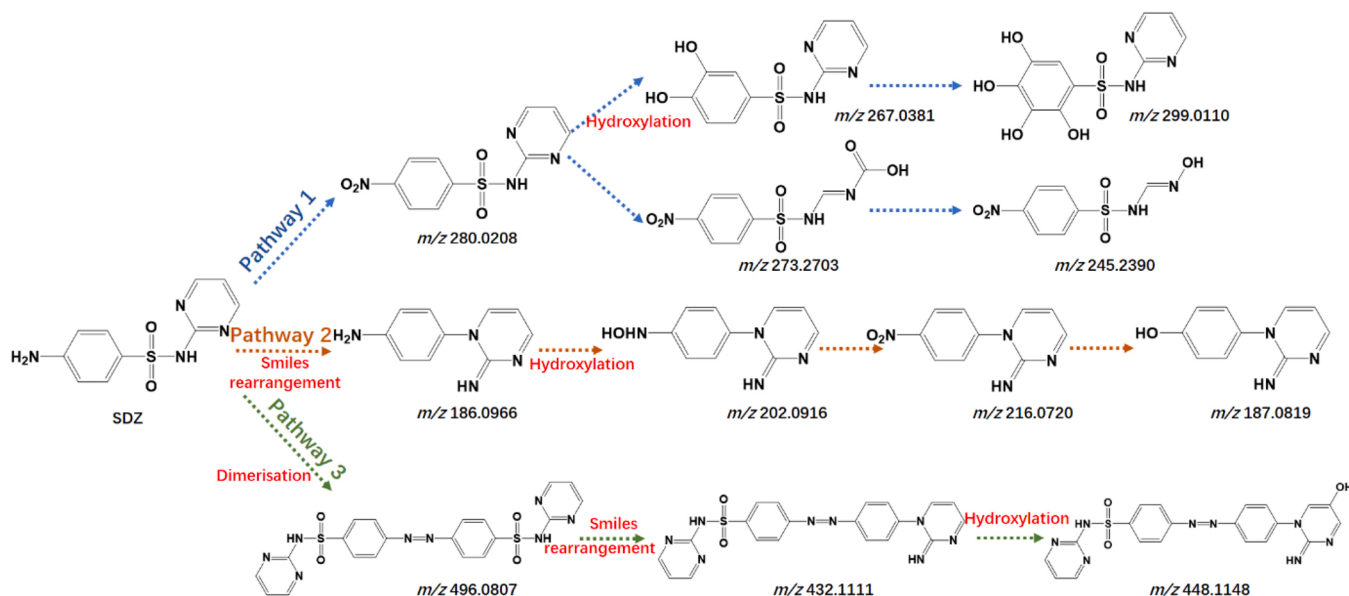


Fig. 7. Proposed pathways of SDZ degradation by PMS under ZIF- $\text{CoN}_3\text{P-C}$ catalysis. Reaction conditions: $[\text{SDZ}] = 20 \text{ mg L}^{-1}$, $[\text{catalyst}] = 0.050 \text{ g L}^{-1}$, $[\text{PMS}] = 1 \text{ mM}$, reaction $\text{pH} = 3.35 \pm 0.1$, temperature $= 20 \pm 1^\circ\text{C}$.

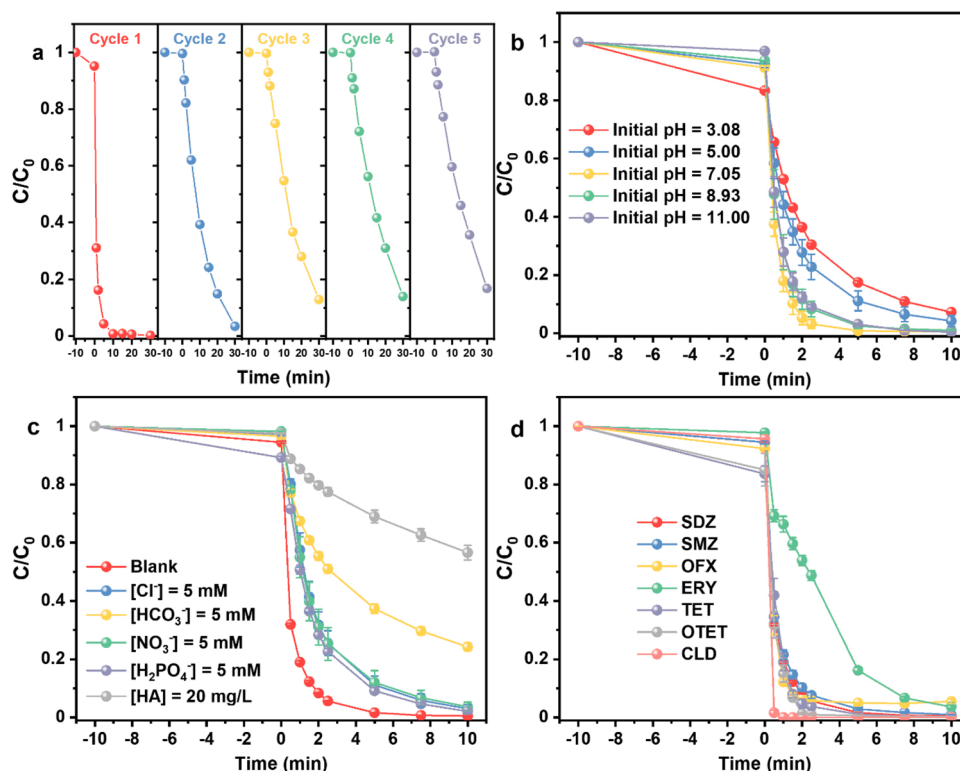


Fig. 8. Experiments on the degradation of SDZ by the ZIF-CoN₃P-C/PMS system: (a) reusability of the catalyst, and effects of the (b) initial pH and (c) anions and HA on the SDZ degradation; (d) removal of various antibiotics by ZIF-CoN₃P-C/PMS. Reaction conditions: [SDZ] (and other antibiotics) = 10 mg L⁻¹, [catalyst] = 0.050 g L⁻¹, [PMS] = 1 mM, reaction pH = 3.35 ± 0.1 (for a, c and d), temperature = 20 ± 1 °C.

atoms in ZIF-CoN₃P-C were rather stable during the cycling tests of PMS activation and SDZ degradation, indicating the stability and reusability of the catalyst.

Various initial solution pH values were set to evaluate the pH tolerance of the ZIF-CoN₃P-C catalyst. As shown in Fig. 8b, the SDZ degradation kinetics are not highly sensitive to solution pH, and the ZIF-CoN₃P-C catalyst exhibits a high performance across a wide pH range. In acidic pH conditions (pH 3.08 and 5.00), the SDZ degradation rates slightly decreased; this was likely due to protonation of the NH₂ moiety in SDZ, as the pH decreased to as low as 2.8 after initially being set to pH 3.08 (Fig. S17). Protonated SDZ would electrostatically repel the positively charged ZIF-CoN₃P-C surface, which could hinder the activation of PMS (Fig. S18). In contrast, under the neutral (pH 7.05) and basic conditions (pH 8.93 and 11.00), the SDZ degradation kinetics were slightly enhanced.

Considering the abundant inorganic anions and natural organic matter in water and wastewater, the effects of the complex matrices on SDZ degradation by PMS with the catalysis of ZIF-CoN₃P-C were evaluated (Fig. 8c). For the relatively high anionic concentrations, the SDZ degradation efficiency slightly decreased when 5 mM of Cl⁻, NO₃⁻ and H₂PO₄⁻ were added. The reaction inhibition was likely induced by the anions migrating to the positively charged surface of ZIF-CoN₃P-C. The inhibitory effect of HCO₃⁻ was more notable, as the SDZ degradation efficiency decreased considerably to 75.7%. On one hand, in contrast to Cl⁻ and NO₃⁻, HCO₃⁻ buffered the solution against changes in pH induced by the addition of the acidic PMS solution [66]. On the other hand, it is noteworthy that HCO₃⁻ (1 × 10⁶ M⁻¹ s⁻¹) and dissociated CO₃²⁻ (5 × 10⁸ M⁻¹ s⁻¹) could react with HO₂[·] and O₂⁻ to act as the quenching agents of HO₂[·] and O₂⁻ [67]. As HO₂[·] and O₂⁻ are the key intermediates prior to the ¹O₂ generation, the recombination of HO₂[·] and O₂⁻ might be inhibited, which would hinder the ¹O₂ production and the subsequent SDZ degradation. The SDZ removal efficiency also significantly decreased when humic acids (HA) was added in the test system.

Although ¹O₂ is less reactive towards HA with a slow oxidation rate (13–22 M⁻¹ s⁻¹), considerable inhibition has been reported on the ¹O₂-dominated reaction [68,69]. The observed reduction in oxidation efficiency in the presence of HA could be caused by the adsorption of the negatively charged HA onto the surface of the catalyst, which hindered the interactions between the catalyst and PMS.

To verify the universality of the novel ZIF-CoN₃P-C catalyst for the PMS-based AOP, the ability of this catalytic system to degrade six commonly used antibiotics (SMZ, OFX, ERY, TET, OTET and CLD) in water was evaluated (Fig. 8d). All six antibiotics were efficiently degraded, despite their different structures and molecular weights. In summary, the ZIF-CoN₃P-C catalyst was found to be stable and able to abate the antibiotic pollution problem in a range of experimental conditions, demonstrating its potential for use in practical water and wastewater treatment.

4. Conclusions

The host-guest technique was used to introduce P into ZIF-based precursors in the CoN₄ sites of Co-based SACs. The EXAFS analysis and chemical characterisations of the product indicate that the CoN₃P sites were constructed with no changes in the carbon matrix, pore structure and surface properties of the catalyst. The P doping effectively enhanced the activity of the catalyst for PMS activation and organic oxidation. SDZ (10 mg L⁻¹) was effectively degraded within 5 min by the ZIF-CoN₃P-C/PMS system, and the reaction rate constant (1.074 × 10⁵ M⁻¹ min⁻¹) was 2.5 times higher than that of ZIF-CoN₄-C (0.420 × 10⁵ M⁻¹ min⁻¹) at a similar Co loading ratio. The quenching experiments and ESR analysis confirm that ¹O₂ is the primary ROS in this PMS-based process, and the ¹O₂ yield from PMS catalysed by ZIF-CoN₃P-C was the highest among the ZIF-derived catalysts. Based on the DFT calculations, the differences in the electron density distribution and ELF indicated that the electrons originally located around the centre Co atom

transferred to the adsorbed PMS molecule, resulting in the breakage of the S–O bond of the PMS and $^1\text{O}_2$ generation. The reaction energy barrier of the $\text{CoN}_3\text{P}/\text{PMS}$ system (-2.47 eV) was found to be lower than that of the CoN_4/PMS system (-2.81 eV), possibly accounting for the enhanced activity of the catalyst towards PMS activation. The $^1\text{O}_2$ that is generated mediates a Smiles rearrangement of SDZ, leading to its degradation. Moreover, the ZIF- CoN_3P -C catalyst exhibited universality and high stability in various reaction conditions. This research presents a novel strategy – based on engineering the coordination environment of Co sites in SACs – for the design and fabrication of efficient catalysts for PMS activation, and subsequent high-efficiency organic oxidation.

CRedit authorship contribution statement

Yubin Zou: Methodology, Investigation, Data curation, Visualization, Writing – original draft. **Jiahui Hu:** Methodology, Investigation. **Bing Li:** Conceptualization, Writing – review & editing, Supervision. **Lin Lin:** Resources, Writing – review & editing. **Yin Li:** Methodology. **Feifei Liu:** Methodology. **Xiao-yan Li:** Funding acquisition, Writing – review & editing, Supervision.

Declaration of Competing Interest

The authors declare that they have no known competing financial interests or personal relationships that could have appeared to influence the work reported in this paper.

Acknowledgements

This work was supported by the National Natural Science Foundation of China (Project No. 51978369), Guangdong Basic and Applied Basic Research Foundation (Project No. 2019B151502034), Shenzhen Knowledge Innovation Program-Basic Research (Project No. JCYJ20180508152004176), and Research Grants Council of the Hong Kong Government (Project Nos. 17210219, T21-711/16R), China.

Appendix A. Supporting information

Supplementary data associated with this article can be found in the online version at [doi:10.1016/j.apcatb.2022.121408](https://doi.org/10.1016/j.apcatb.2022.121408).

References

- [1] S. Gupta, G. Arango-Argoty, L. Zhang, A. Pruden, P. Vikesland, Identification of discriminatory antibiotic resistance genes among environmental resistomes using extremely randomized tree algorithm, *Microbiome* 7 (2019) 123.
- [2] B. Li, T. Zhang, Biodegradation and adsorption of antibiotics in the activated sludge process, *Environ. Sci. Technol.* 44 (2010) 3468–3473.
- [3] I.L. Pepper, J.P. Brooks, C.P. Gerba, Antibiotic resistant bacteria in municipal wastes: Is there reason for concern? *Environ. Sci. Technol.* 52 (2018) 3949–3959.
- [4] Y.-G. Zhu, T.A. Johnson, J.-Q. Su, M. Qiao, G.-X. Guo, R.D. Stedtfeld, S. A. Hashsham, J.M. Tiedje, Diverse and abundant antibiotic resistance genes in Chinese swine farms, *Proc. Natl. Acad. Sci. USA* 110 (2013) 3435–3440.
- [5] M. Pei, B. Zhang, Y. He, J. Su, K. Gin, O. Lev, G. Shen, S. Hu, State of the art of tertiary treatment technologies for controlling antibiotic resistance in wastewater treatment plants, *Environ. Int.* 131 (2019), 105026.
- [6] P. Grenni, V. Ancona, A. Barra Caracciolo, Ecological effects of antibiotics on natural ecosystems: a review, *Microchem. J.* 136 (2018) 25–39.
- [7] J. Cui, L. Fu, B. Tang, L. Bin, P. Li, S. Huang, F. Fu, Occurrence, ecotoxicological risks of sulfonamides and their acetylated metabolites in the typical wastewater treatment plants and receiving rivers at the Pearl River Delta, *Sci. Total Environ.* 709 (2020), 136192.
- [8] M.B. Ahmed, J.L. Zhou, H.H. Ngo, W. Guo, N.S. Thomaidis, J. Xu, Progress in the biological and chemical treatment technologies for emerging contaminant removal from wastewater: a critical review, *J. Hazard. Mater.* 323 (2017) 274–298.
- [9] Z. Wu, J. Fang, Y. Xiang, C. Shang, X. Li, F. Meng, X. Yang, Roles of reactive chlorine species in trimethoprim degradation in the UV/chlorine process: Kinetics and transformation pathways, *Water Res.* 104 (2016) 272–282.
- [10] H. Zhao, Y. Wang, Y. Wang, T. Cao, G. Zhao, Electro-Fenton oxidation of pesticides with a novel $\text{Fe}_3\text{O}_4/\text{Fe}_2\text{O}_3$ /activated carbon aerogel cathode: High activity, wide pH range and catalytic mechanism, *Appl. Catal. B* 125 (2012) 120–127.
- [11] C.K. Duisterberg, T.D. Waite, Process optimization of Fenton oxidation using kinetic modeling, *Environ. Sci. Technol.* 40 (2006) 4189–4195.
- [12] B.C. Hodges, E.L. Cates, J.-H. Kim, Challenges and prospects of advanced oxidation water treatment processes using catalytic nanomaterials, *Nat. Nanotechnol.* 13 (2018) 642–650.
- [13] J. Lee, U. von Gunten, J.H. Kim, Persulfate-based advanced oxidation: critical assessment of opportunities and roadblocks, *Environ. Sci. Technol.* 54 (2020) 3064–3081.
- [14] Q. Yang, X. Yang, Y. Yan, C. Sun, H. Wu, J. He, D. Wang, Heterogeneous activation of peroxymonosulfate by different ferromanganese oxides for tetracycline degradation: structure dependence and catalytic mechanism, *Chem. Eng. J.* 348 (2018) 263–270.
- [15] S. Indrawirawan, H. Sun, X. Duan, S. Wang, Nanocarbons in different structural dimensions (0–3D) for phenol adsorption and metal-free catalytic oxidation, *Appl. Catal. B* 179 (2015) 352–362.
- [16] X. Han, W. Zhang, S. Li, C. Cheng, L. Zhou, Q. Jia, G. Xiu, Efficient activation of peroxymonosulfate by $\text{MnS}/\text{Fe-MOF}$ hybrid catalyst for sulfadiazine degradation: synergistic effects and mechanism, *Sep. Purif. Technol.* 287 (2022), 120509.
- [17] C. Ling, S. Wu, T. Dong, H. Dong, Z. Wang, Y. Pan, J. Han, Sulfadiazine removal by peroxymonosulfate activation with sulfide-modified microscale zero-valent iron: Major radicals, the role of sulfur species, and particle size effect, *J. Hazard. Mater.* 423 (2022), 127082.
- [18] B. Qiao, A. Wang, X. Yang, L.F. Allard, Z. Jiang, Y. Cui, J. Liu, J. Li, T. Zhang, Single-atom catalysis of CO oxidation using $\text{Pt1}/\text{FeOx}$, *Nat. Chem.* 3 (2011) 634–641.
- [19] L. Zhang, Y. Ren, W. Liu, A. Wang, T. Zhang, Single-atom catalyst: a rising star for green synthesis of fine chemicals, *Natl. Sci. Rev.* 5 (2018) 653–672.
- [20] S. Mitchell, E. Vorobyeva, J. Pérez-Ramírez, The multifaceted reactivity of single-atom heterogeneous catalysts, *Angew. Chem. Int. Ed.* 57 (2018) 15316–15329.
- [21] D. Yang, B.C. Gates, Uniformity begets selectivity, *Nat. Mater.* 16 (2017) 703–704.
- [22] Z. Li, S. Ji, Y. Liu, X. Cao, S. Tian, Y. Chen, Z. Niu, Y. Li, Well-defined materials for heterogeneous catalysis: From nanoparticles to isolated single-atom sites, *Chem. Rev.* 120 (2020) 623–682.
- [23] L.-S. Zhang, X.-H. Jiang, Z.-A. Zhong, L. Tian, Q. Sun, Y.-T. Cui, X. Lu, J.-P. Zou, S.-L. Luo, Carbon nitride supported high-loading Fe single-atom catalyst for activation of peroxymonosulfate to generate $^1\text{O}_2$ with 100% selectivity, *Angew. Chem. Int. Ed.* 60 (2021) 21751–21755.
- [24] Z. Zhao, W. Zhou, D. Lin, L. Zhu, B. Xing, Z. Liu, Construction of dual active sites on diatomic metal (FeCo-N/C-x) catalysts for enhanced Fenton-like catalysis, *Appl. Catal. B* 309 (2022), 121256.
- [25] N. Jiang, H. Xu, L. Wang, J. Jiang, T. Zhang, Nonradical oxidation of pollutants with single-atom-Fe(III)-activated persulfate: Fe(V) being the possible intermediate oxidant, *Environ. Sci. Technol.* 54 (2020) 14057–14065.
- [26] A. Schoedel, M. Li, D. Li, M. O’Keeffe, O.M. Yaghi, Structures of metal-organic frameworks with rod secondary building units, *Chem. Rev.* 116 (2016) 12466–12535.
- [27] X.X. Ward, D.A. Cullen, Y.T. Pan, S. Hwang, M. Wang, Z. Feng, J. Wang, M. H. Engelhard, H. Zhang, Y. He, Y. Shao, D. Su, K.L. More, J.S. Spendlow, G. Wu, Nitrogen-coordinated single cobalt atom catalysts for oxygen reduction in proton exchange membrane fuel cells, *Adv. Mater.* 30 (2018), 1706758.
- [28] N. Cheng, L. Ren, X. Xu, Y. Du, S.X. Dou, Recent development of zeolitic imidazolate frameworks (ZIFs) derived porous carbon based materials as electrocatalysts, *Adv. Energy Mater.* 8 (2018), 1801257.
- [29] X.F. Lu, B.Y. Xia, S.Q. Zang, X.W.D. Lou, Metal-organic frameworks based electrocatalysts for the oxygen reduction reaction, *Angew. Chem. Int. Ed.* 59 (2020) 4634–4650.
- [30] X. Han, X. Ling, Y. Wang, T. Ma, C. Zhong, W. Hu, Y. Deng, Generation of nanoparticle, atomic-cluster, and single-atom cobalt catalysts from zeolitic imidazole frameworks by spatial isolation and their use in zinc–air batteries, *Angew. Chem. Int. Ed.* 58 (2019) 5359–5364.
- [31] F. Xiao, G.-L. Xu, C.-J. Sun, M. Xu, W. Wen, Q. Wang, M. Gu, S. Zhu, Y. Li, Z. Wei, X. Pan, J. Wang, K. Amine, M. Shao, Nitrogen-coordinated single iron atom catalysts derived from metal organic frameworks for oxygen reduction reaction, *Nano Energy* 61 (2019) 60–68.
- [32] Z. Lin, H. Huang, L. Cheng, Y. Yang, R. Zhang, Q. Chen, Atomically dispersed Mn within carbon frameworks as high-performance oxygen reduction electrocatalysts for zinc–air battery, *ACS Sustain. Chem. Eng.* 8 (2020) 427–434.
- [33] J. He, Y. Wan, W. Zhou, ZIF-8 derived Fe–N coordination moieties anchored carbon nanocubes for efficient peroxymonosulfate activation via non-radical pathways: Role of FeNx sites, *J. Hazard. Mater.* 405 (2021), 124199.
- [34] X. Mi, P. Wang, S. Xu, L. Su, H. Zhong, H. Wang, Y. Li, S. Zhan, Almost 100% peroxymonosulfate conversion to singlet oxygen on single-atom CoN_{2+2} sites, *Angew. Chem. Int. Ed.* 60 (2021) 4588–4593.
- [35] J. Wan, Z. Zhao, H. Shang, B. Peng, W. Chen, J. Pei, L. Zheng, J. Dong, R. Cao, R. Sarangi, Z. Jiang, D. Zhou, Z. Zhuang, J. Zhang, D. Wang, Y. Li, In situ phosphatizing of triphenylphosphine encapsulated within metal-organic frameworks to design atomic $\text{Co}_1\text{-P}_1\text{N}_3$ interfacial structure for promoting catalytic performance, *J. Am. Chem. Soc.* 142 (2020) 8431–8439.
- [36] H. Shang, X. Zhou, J. Dong, A. Li, X. Zhao, Q. Liu, Y. Lin, J. Pei, Z. Li, Z. Jiang, D. Zhou, L. Zheng, Y. Wang, J. Zhou, Z. Yang, R. Cao, R. Sarangi, T. Sun, X. Yang, X. Zheng, W. Yan, Z. Zhuang, J. Li, W. Chen, D. Wang, J. Zhang, Y. Li, Engineering unsymmetrically coordinated $\text{Cu-S}_2\text{N}_3$ single atom sites with enhanced oxygen reduction activity, *Nat. Commun.* 11 (2020) 3049.
- [37] G. Kresse, J. Furthmüller, Efficient iterative schemes for ab initio total-energy calculations using a plane-wave basis set, *Phys. Rev. B* 54 (1996) 11169–11186.
- [38] S. Grimme, J. Antony, S. Ehrlich, H. Krieg, A consistent and accurate ab initio parametrization of density functional dispersion correction (DFT-D) for the 94 elements H–Pu, *J. Chem. Phys.* 132 (2010), 154104.

- [39] W. Tang, E. Sanville, G. Henkelman, A grid-based Bader analysis algorithm without lattice bias, *J. Phys. Condens. Matter* 21 (2009), 084204.
- [40] B. Silvi, A. Savin, Classification of chemical bonds based on topological analysis of electron localization functions, *Nature* 371 (1994) 683–686.
- [41] N.D. Lang, W. Kohn, Theory of metal surfaces: Work function, *Phys. Rev. B* 3 (1971) 1215–1223.
- [42] A. Sadezky, H. Muckenhuber, H. Grothe, R. Niessner, U. Pöschl, Raman microspectroscopy of soot and related carbonaceous materials: Spectral analysis and structural information, *Carbon* 43 (2005) 1731–1742.
- [43] M.A. Pimenta, G. Dresselhaus, M.S. Dresselhaus, L.G. Cançado, A. Jorio, R. Saito, Studying disorder in graphite-based systems by Raman spectroscopy, *Phys. Chem. Chem. Phys.* 9 (2007) 1276–1290.
- [44] J. Li, M. Li, H. Sun, Z. Ao, S. Wang, S. Liu, Understanding of the oxidation behavior of benzyl alcohol by peroxymonosulfate via carbon nanotubes activation, *ACS Catal.* 10 (2020) 3516–3525.
- [45] Z. Song, M. Wang, Z. Wang, Y. Wang, R. Li, Y. Zhang, C. Liu, Y. Liu, B. Xu, F. Qi, Insights into heteroatom-doped graphene for catalytic ozonation: Active centers, reactive oxygen species evolution, and catalytic mechanism, *Environ. Sci. Technol.* 53 (2019) 5337–5348.
- [46] M. Mahato, R. Tabassian, V.H. Nguyen, S. Oh, S. Nam, W.-J. Hwang, I.-K. Oh, CTF-based soft touch actuator for playing electronic piano, *Nat. Commun.* 11 (2020) 5358.
- [47] B. Jiang, Y. Yao, R. Xie, D. Dai, W. Lu, W. Chen, L. Zhang, Enhanced generation of reactive oxygen species for efficient pollutant elimination catalyzed by hemin based on persistent free radicals, *Appl. Catal. B* 183 (2016) 291–297.
- [48] J. Xiong, X. Li, J. Huang, X. Gao, Z. Chen, J. Liu, H. Li, B. Kang, W. Yao, Y. Zhu, CN/rGO@BPQDs high-low junctions with stretching spatial charge separation ability for photocatalytic degradation and H₂O₂ production, *Appl. Catal. B* 266 (2020), 118602.
- [49] F. Li, M. Han, Y. Jin, L. Zhang, T. Li, Y. Gao, C. Hu, Internal electric field construction on dual oxygen group-doped carbon nitride for enhanced photodegradation of pollutants under visible light irradiation, *Appl. Catal. B* 256 (2019), 117705.
- [50] Y. Zhao, H. Zhou, X. Zhu, Y. Qu, C. Xiong, Z. Xue, Q. Zhang, X. Liu, F. Zhou, X. Mou, W. Wang, M. Chen, Y. Xiong, X. Lin, Y. Lin, W. Chen, H.-J. Wang, Z. Jiang, L. Zheng, T. Yao, J. Dong, S. Wei, W. Huang, L. Gu, J. Luo, Y. Li, Y. Wu, Simultaneous oxidative and reductive reactions in one system by atomic design, *Nat. Catal.* 4 (2021) 134–143.
- [51] L. Cao, Q. Luo, W. Liu, Y. Lin, X. Liu, Y. Cao, W. Zhang, Y. Wu, J. Yang, T. Yao, S. Wei, Identification of single-atom active sites in carbon-based cobalt catalysts during electrocatalytic hydrogen evolution, *Nat. Catal.* 2 (2019) 134–141.
- [52] H. Funke, A.C. Scheinost, M. Chukalina, Wavelet analysis of extended x-ray absorption fine structure data, *Phys. Rev. B* 71 (2005), 094110.
- [53] Y. Chen, R. Gao, S. Ji, H. Li, K. Tang, P. Jiang, H. Hu, Z. Zhang, H. Hao, Q. Qu, X. Liang, W. Chen, J. Dong, D. Wang, Y. Li, Atomic-level modulation of electronic density at cobalt single-atom sites derived from metal-organic frameworks: Enhanced oxygen reduction performance, *Angew. Chem. Int. Ed. Engl.* 60 (2021) 3212–3221.
- [54] P. Sun, H. Liu, M. Feng, Z. Zhai, Y. Fang, X. Zhang, V.K. Sharma, Strategic combination of N-doped graphene and g-C₃N₄: Efficient catalytic peroxymonosulfate-based oxidation of organic pollutants by non-radical-dominated processes, *Appl. Catal. B* 272 (2020), 119005.
- [55] G.P. Anipsitakis, D.D. Dionysiou, Radical generation by the interaction of transition metals with common oxidants, *Environ. Sci. Technol.* 38 (2004) 3705–3712.
- [56] Y. Zong, X. Guan, J. Xu, Y. Feng, Y. Mao, L. Xu, H. Chu, D. Wu, Unraveling the overlooked involvement of high-valent cobalt-oxo species generated from the cobalt(II)-activated peroxymonosulfate process, *Environ. Sci. Technol.* 54 (2020) 16231–16239.
- [57] K.Z. Huang, H. Zhang, Direct electron-transfer-based peroxymonosulfate activation by iron-doped manganese oxide (δ -MnO₂) and the development of galvanic oxidation processes (GOPs), *Environ. Sci. Technol.* 53 (2019) 12610–12620.
- [58] X. Li, X. Huang, S. Xi, S. Miao, J. Ding, W. Cai, S. Liu, X. Yang, H. Yang, J. Gao, J. Wang, Y. Huang, T. Zhang, B. Liu, Single cobalt atoms anchored on porous N-doped graphene with dual reaction sites for efficient Fenton-like catalysis, *J. Am. Chem. Soc.* 140 (2018) 12469–12475.
- [59] P. Bilski, K. Reszka, M. Bilska, C.F. Chignell, Oxidation of the spin trap 5,5-dimethyl-1-pyrroline N-oxide by singlet oxygen in aqueous solution, *J. Am. Chem. Soc.* 118 (1996) 1330–1338.
- [60] C. Chen, F. Li, H.-L. Chen, M.G. Kong, Interaction between air plasma-produced aqueous ¹O₂ and the spin trap DMPO in electron spin resonance, *Phys. Plasmas* 24 (2017), 103501.
- [61] Z. Yang, J. Qian, A. Yu, B. Pan, Singlet oxygen mediated iron-based Fenton-like catalysis under nanoconfinement, *Proc. Natl. Acad. Sci. USA* 116 (2019) 6659–6664.
- [62] P. Raja, A. Bozzi, H. Mansilla, J. Kiwi, Evidence for superoxide-radical anion, singlet oxygen and OH-radical intervention during the degradation of the lignin model compound (3-methoxy-4-hydroxyphenylmethylcarbinol), *J. Photochem. Photobiol. A* 169 (2005) 271–278.
- [63] C. Gao, Y. Su, X. Quan, V.K. Sharma, S. Chen, H. Yu, Y. Zhang, J. Niu, Electronic modulation of iron-bearing heterogeneous catalysts to accelerate Fe(III)/Fe(II) redox cycle for highly efficient Fenton-like catalysis, *Appl. Catal. B* (2020), 119016.
- [64] M. Feng, J.C. Baum, N. Nesnas, Y. Lee, C.-H. Huang, V.K. Sharma, Oxidation of sulfonamide antibiotics of six-membered heterocyclic moiety by ferrate(VI): Kinetics and mechanistic insight into SO₂ extrusion, *Environ. Sci. Technol.* 53 (2019) 2695–2704.
- [65] Y.-Y. Guo, Z.-H. Li, T.-Y. Xia, Y.-L. Du, X.-M. Mao, Y.-Q. Li, Molecular mechanism of azoxy bond formation for azoxymycins biosynthesis, *Nat. Commun.* 10 (2019) 4420.
- [66] Y. Wang, M. Liu, X. Zhao, D. Cao, T. Guo, B. Yang, Insights into heterogeneous catalysis of peroxymonosulfate activation by boron-doped ordered mesoporous carbon, *Carbon* 135 (2018) 238–247.
- [67] B.H.J. Bielski, D.E. Cabelli, R.L. Arudi, A.B. Ross, Reactivity of HO₂/O₂⁻ radicals in aqueous solution, *J. Phys. Chem. Ref. Data* 14 (1985) 1041–1100.
- [68] P. Shao, J. Tian, F. Yang, X. Duan, S. Gao, W. Shi, X. Luo, F. Cui, S. Luo, S. Wang, Identification and regulation of active sites on nanodiamonds: establishing a highly efficient catalytic system for oxidation of organic contaminants, *Adv. Funct. Mater.* 28 (2018), 1705295.
- [69] Y. Yao, H. Yin, M. Gao, Y. Hu, H. Hu, M. Yu, S. Wang, Electronic structure modulation of covalent organic frameworks by single-atom Fe doping for enhanced oxidation of aqueous contaminants, *Chem. Eng. Sci.* 209 (2019), 115211.